Real-Time Low-Level Wind and Temperature Analysis Using Single WSR-88D Data

JUANZHEN SUN AND N. ANDREW CROOK

National Center for Atmospheric Research, Boulder, Colorado*

(Manuscript received 24 February 2000, in final form 2 October 2000)

ABSTRACT

A four-dimensional variational Doppler radar analysis system (VDRAS) has been developed and implemented at a weather forecast office to produce real-time boundary layer wind and temperature analyses using WSR-88D radar data. This paper describes significant changes made to convert VDRAS from a research tool to a real-time analysis system and presents results of low-level wind and temperature analysis using operational radar data. In order to produce continuous analyses with time, VDRAS was implemented with a cycling procedure, in which the analysis from the previous cycle is used as a first guess and background for the next cycle. Other enhancements in this real-time system include direct assimilation of data on constant elevation angle levels, addition of mesonet observations, inclusion of an analysis background term, and continuous updating of lateral boundary conditions.

An observed case of a line of storms and strong outflow is used to examine the performance of the real-time analysis system and its sensitivity to various system changes. The quality of the analysis for this case is examined by comparing the subsequent 90-min forecast with the observed radial velocity. It is shown that the forecast initialized using the VDRAS analysis outperforms persistence and a forecast using a mesoscale analysis. The accuracy of the retrieved wind in six convective cases is also verified against automated weather reports from commercial aircraft data. The verification shows an average difference of 3.3 m s^{-1} over these six cases.

1. Introduction

As the resolution of numerical weather prediction models steadily increases, it is recognized that radar observations will play an important role in future convective- and mesoscale data assimilation systems. The Weather Surveillance Radar-1988 Doppler (WSR-88D) network provides measurements of radial velocity and reflectivity with high spatial and temporal resolution. While the WSR-88D network has had a profound impact on severe weather detection and warning in National Weather Service (NWS) Forecast Offices (NWSFOs, Telesetsky 1995), its role in initializing storm-scale numerical prediction models and quantitative precipitation forecasting remains to be explored. One of the major challenges in using radar data in short-term forecasting is the retrieval of unobserved meteorological fields such as the crossbeam velocity, temperature, and microphysical variables. Due to the distant spacing of the radars in the WSR-88D network, it is impossible to obtain dual-Doppler coverage in most areas. Hence, the feasibility of storm-scale weather prediction will depend on whether the detailed meteorological fields can be successfully retrieved from single-Doppler radar data.

In the last decade, active research has been undertaken to infer detailed meteorological information from single-Doppler radar data. Most of the methods developed so far focus on the determination of three-dimensional boundary layer winds using data from clear air returns (Rinehart 1979; Tuttle and Foote 1990; Zhang and Gal-Chen 1996; Xu et al. 1993; Laroche and Zawadsky 1994; Shapiro et al. 1995). Although the individual approaches are different, these methods all rely on the assumption that reflectivity (or radial velocity) acts as a passive tracer and hence can be tracked to determine the flow field. The retrieved boundary layer winds can then be used to derive the thermodynamic fields with the aid of the Navier–Stokes equations (Gal-Chen 1978; Hane and Scott 1978).

Methods that combine observations and the full set of fluid dynamics equations have also been examined in recent years. A forward insertion procedure was developed by Liou (1990) that consists of radial velocity insertion, model prediction, and thermodynamic retrieval. Another technique that exploits the inclusion of a numerical model in the retrieval is the four-dimensional

---

* The National Center for Atmospheric Research is sponsored by the National Science Foundation.

Corresponding author address: Dr. Juanzhen Sun, National Center for Atmospheric Research, P.O. Box 3000, Boulder, CO 80301.
E-mail: sunj@ucar.edu

variational (4DVAR) adjoint technique (Sun et al. 1991). By applying optimal control theory, this method seeks a solution that satisfies the fluid dynamic equations, while simultaneously finding a best fit to all the observations in a specified assimilation window. Unlike the simple techniques mentioned above, the 4DVAR technique can retrieve not only the three-dimensional boundary layer wind but also the thermodynamical fields.

The 4DVAR adjoint retrieval technique was first examined by Wolfsberg (1987) and Sun et al. (1991) using a Boussinesq model and simulated boundary layer turbulence data. The work was one of the first applications of the adjoint method to atmospheric data assimilation (Le Dimet and Talagrand 1986; Lewis and Derber 1985; Courtier and Talagrand 1987; Talagrand and Courtier 1987). The four-dimensional variational Doppler radar analysis system (VDRAS) was improved and tested on observations of a gust front produced by a thunderstorm outflow (Sun and Crook 1994) and gave promising results. VDRAS was further developed to retrieve the dynamical and microphysical structure within convective storms. Sun and Crook (1997, 1998) showed that VDRAS was able to retrieve the three-dimensional wind, thermodynamical, and microphysical fields in a Florida airmass storm. Wu et al. (2000) applied this system to a supercell storm observed during the Microburst and Severe Thunderstorm (MIST) project and found it was able to retrieve all the prominent features of the storm although problems existed in the detailed structure of the retrieval. Obviously, further study is required before VDRAS with microphysical retrieval can be used operationally.

With the possibility of retrieving high-resolution fields from operational Doppler radars, methods are presently under development for using these data to forecast thunderstorm initiation and evolution. Attempts to initialize storm-scale numerical models using retrieved fields from single-Doppler radars and to forecast thunderstorm evolution have been made by a number of investigators (Weygandt 1998; Gao et al. 1998). We have recently performed a 2-h, after-the-fact, forecast of the Buffalo Creek, Colorado, flash flood case using initial conditions obtained from VDRAS (Warner et al. 2000). Although a number of problems remain to be investigated, the results show some promise. Besides the numerical forecasting technique, a number of knowledge-based expert systems are also under development for very short-term forecasting of thunderstorms (Roberts et al. 1999). The retrieved wind and temperature information can be one of the important inputs for these systems.

The simulated data study and the applications of VDRAS to data from research radars have provided us a good understanding of the performance and sensitivity of VDRAS under various conditions. However, our ultimate goal is to retrieve the unobserved meterological variables from operational radar data. With current computing power, it is not yet possible to assimilate operational radar data observed in the entire troposphere using a full cloud model. Therefore, as a first step in the real-time application of VDRAS, we implemented a dry version of the VDRAS system to assimilate boundary layer data and focused mainly on the clear air returns in the low level. In the summer of 1998, the dry version of VDRAS was implemented in a real-time setting at the NWS Washington, D.C.–Baltimore weather forecast office at Sterling, Virginia, as one of the major components of National Center for Atmospheric Research's (NCAR) Thunderstorm Nowcasting System [also referred to as the Auto-Nowcaster (Roberts et al. 1999)]. In addition to providing a display of the current low-level wind for the forecasters, the analysis wind and convergence field can also be input to the Auto-Nowcaster. VDRAS was run on a dedicated PC in the forecast office to produce boundary layer wind and temperature analyses by assimilating data from the KLWX WSR-88D radar at Sterling. Since real-time analysis using operational radar data has different considerations from research-oriented studies, significant changes needed to be made to VDRAS before and during the field programs. One of the major changes to VDRAS was the implementation of a continuous 4DVAR cycling procedure. Other changes include direct assimilation of data on constant elevation angles, addition of an analysis background, inclusion of mesonet data, and modification of the boundary conditions.

In this paper, we describe the recent improvements in the real-time system and show some results using WSR-88D radar observations. In section 2, we give a brief description of the VDRAS technique with a focus on changes that have been made in the real-time system. In section 3, the performance of the retrieval system is examined using a case of a line of storms and a thunderstorm outflow. In section 4, verification of the retrieved fields using automated weather reports from commercial aircraft (ACARS) is discussed. Conclusions are drawn in section 5.

2. Description of the 4DVAR analysis technique

VDRAS was designed to assimilate a time series of radar observations (radial velocity and reflectivity) from single- or multiple-Doppler radars. A cloud-scale numerical model is used to represent the evolution of the motion in the atmosphere. In the dry version of VDRAS that was used in our real-time application, the numerical model includes four prognostic equations: one each for the three velocity components (u, v, and w), and the potential temperature (θ). The pressure (p) is diagnosed through a Poisson equation. In order to assimilate reflectivity data, an additional equation, the conservation equation for reflectivity (dBZ), is included in the numerical model (Sun and Crook 1994). The lateral boundary conditions of the numerical model are open, such that the inflow is prescribed (see section 2e for the specification of the inflow boundary conditions) and the outflow is extrapolated using the closest inner two grid points. The top and bottom boundary conditions are set to zero for vertical velocity, and all other variables are defined such that their derivatives vanish.

By fitting the model to observations over a specified time period, a set of optimal initial conditions of the constraining numerical model can be obtained. A cost function, which measures the misfit between the model variables and both the observations and a prior estimate, is defined by

$$J = J_o + J_b + J_p. \tag{2.1}$$

The first term J_o in Eq. (2.1) represents the discrepancy from the radar observations. It can be written in a general vector form as

$$J_o = \sum_{0\le k\le N} (\mathbf{H}\mathbf{x}_k - \mathbf{y}_k^o)^{\mathrm{T}}\mathbf{R}^{-1}(\mathbf{H}\mathbf{x}_k - \mathbf{y}_k^o), \tag{2.2}$$

where k is the time index, $\mathbf{x}_k$ is the state vector, and $\mathbf{y}_k^o$ is the observation vector. In addition, $\mathbf{H}$ is the observation operator, and $\mathbf{R}$ is the error covariance matrix, which includes two sources of error: observation error and error in the observation operator. In our current system, the matrix $\mathbf{R}$ is assumed diagonal (discussion concerning this matrix will be given in section 5). Since $\mathbf{x}_k$ and $\mathbf{y}_k^o$ can be different variables and on different grids, the observation operator $\mathbf{H}$ represents both an analytical function that relates the model variables (i.e., u, v, and w) to the observation variables (i.e., radial velocity v_r) and a transformation between the different grid meshes. Under the assumption that the errors in the observations are not correlated, Eq. (2.2) can be written in the following form:

$$J_o = \sum_{\sigma,t} \{\eta_v[F(v_r) - v_r^o]^2 + \eta_z[F(Z) - Z^o]^2\}, \tag{2.3}$$

where v_r^o and Z^o represent the input radial velocity and reflectivity; v_r and Z are their model counterparts, respectively; F stands for the function that transforms a variable from its model grid to the input data grid and will be described later in this section; and η_v and η_Z are weighting coefficients for radial velocity and reflectivity, respectively, and they are specified based on the typical scales of these fields. They were, respectively, set to 1 and 0.5 in the Sterling field testing and in all of the experiments presented here unless they are otherwise specified. Here, σ and t stand for the spatial and temporal extents of the assimilation window. Reflectivity is one of the model prognostic variables while the model radial velocity has to be computed from the model Cartesian velocity components using the following relation:

$$v_r = \frac{x - x_{\mathrm{rad}}}{r}u + \frac{y - y_{\mathrm{rad}}}{r}v + \frac{z - z_{\mathrm{rad}}}{r}(w - V_T). \tag{2.4}$$

In (2.4), r represents the distance between a model grid point (x, y, z) and the radar location $(x_{\mathrm{rad}}, y_{\mathrm{rad}}, z_{\mathrm{rad}})$ and V_T is the terminal velocity for rain. The terminal velocity is estimated using the reflectivity data through the following relation (Sun and Crook 1997):

$$V_T = 5.4 \times 10^{0.00714(\mathrm{dB}Z - 43.1)}. \tag{2.5}$$

The second term, J_b, in Eq. (2.1) is the background term. It measures the discrepancy from the previous analysis or forecast and is defined by

$$J_b = (\mathbf{x}_0 - \mathbf{x}_0^b)^{\mathrm{T}}\mathbf{B}^{-1}(\mathbf{x}_0 - \mathbf{x}_0^b), \tag{2.6}$$

where $\boldsymbol{x}_0^b$ is the background state vector and B is the background error covariance matrix. A common practice in data assimilation is to use the numerical forecast from the previous analysis–forecast cycle as the background of the current cycle. However, in our system, we use the analysis from the previous 4DVAR cycle as the background since our cycle consists of analysis only. Although the use of the previous analysis generates a correlation between the background and the observations, this correlation is neglected in the cost function. In the next section, we will show that using an analysis background can produce better results than using a background from a previous forecast.

The third term, J_p, is the spatial and temporal smoothness penalty term, which takes the following form:

$$J_p = \sum_{\sigma,t,i,j} \alpha_{1i}\left(\frac{\partial A_j}{\partial x_i}\right)^2 + \alpha_{2i}\left(\frac{\partial^2 A_j}{\partial x_i^2}\right)^2 + \alpha_{3i}\left(\frac{\partial A_j}{\partial t}\right)^2 + \alpha_{4i}\left(\frac{\partial^2 A_j}{\partial t^2}\right)^2, \tag{2.7}$$

where A_j represents any of the model-dependent variables and x_i represents the spatial dimension (x, y, z). Similar smoothness penalty functions have been previously used by other investigators (e.g., Wahba and Wendelberger 1980; Long and Thacker 1989). The weighting coefficients in the penalty terms are determined in a trial-and-error fashion. More discussion on the determination of these coefficients will be given in the next section. Since the background error term is used in the system, the addition of the spatial smoothness penalty term may seem redundant. In the next section, we will compare the effects of these terms and give some discussion.

a. Data preprocessing and quality control

The WSR-88D level II data have a range gate spacing of 250 m for radial velocity and 1 km for reflectivity and an azimuth spacing of 1° for both variables. In storm mode, each radar volume contains nine elevation scans: 0.5°, 1.5°, 2.4°, 3.4°, 4.3°, 6.0°, 9.9°, 14.6°, and 19.5°. The resolution in the vertical direction is range dependent, becoming rather poor at large distances from the radar. At a range distance of 75 km, there are only three vertical data points in the lowest 2.6 km, which is the depth of the analysis domain. However, the horizontal resolution of the data is much better than that of the model grid. Therefore, the original radar data are interpolated to a 1-km Cartesian grid in the horizontal before they are read by VDRAS. Most of the quality control procedures are performed on the 1-km data. After quality control, the data are further interpolated to the model 3-km grid in the horizontal while remaining on the constant elevation angle levels in the vertical.

Velocity unfolding is performed on the data ingest stream using the algorithm developed by Jing and Wiener (1993). In order to remove data contaminated by nearby ground clutter as well as clutter resulting from anomalous propagation, any velocity data with values less than 0.25 m s^{-1} and the corresponding reflectivity data were removed, since one of the distinct features of ground clutter and anomalous propagation is a velocity near zero. A final quality check is to remove any remaining spurious data by computing the deviation of each data point from its local mean. Within a specified local region, a mean of all the data points is calculated. The data value at the central point is compared to this mean, and if the difference exceeds a specified value, this central value is removed.

Since the reflectivity return from hydrometeors is not conserved, these data need to be removed or a source term added to the reflectivity equation. For simplicity, we only account for the effect of precipitation fallout. We use a threshold value of 12 dBZ to distinguish reflectivity return from clear air and from hydrometeors; that is, any reflectivity data greater than 12 dBZ are regarded as returns from hydrometeors. Tests have shown that either removing the data from hydrometeor return or using the parameterized source term does not make a significant difference due to the fact that the reflectivity data plays a relatively unimportant role in the retrieval, as will be shown in the next section.

b. Direct assimilation of PPI data

An important improvement to VDRAS was to enable it to read and assimilate radar data on constant elevation levels in the vertical. Due to the poor vertical resolution of the WSR-88D data, a vertical interpolation of the data from the constant elevation levels to the model Cartesian levels can result in large errors. The direct assimilation of the plan position indicator (PPI) data with no vertical interpolation allows an optimal interpolation within the context of the 4DVAR formulation. For consideration of computational efficiency, however, we did not choose to assimilate the radar data in the original spherical polar coordinate sampling grid. Instead, on each constant elevation angle surface, data were interpolated from the 2D polar sampling grid to a 2D Cartesian grid. The justification for this processing procedure is that the poorest polar sampling resolution of the radar data (approximately 2 km at 120 km from the radar, which is the farthest range distance in the analysis domain) is still better than the resolution of the model grid (3 km). From now on, we will refer to the interpolated PPI data as observations.

Since the input PPI data are on constant elevation levels, an observation operator H must be formulated to map the model variables from the model grid to the data grid such that the differences between the observations and the model solution can be computed in the cost function. Based on radar principles, the following relation is used to transform the data from the model vertical levels to the elevation angle levels:

$$v_{r,e} = F(v_r) = \frac{\sum G v_r \Delta z}{\sum G \Delta z}, \qquad (2.8)$$

where $v_{r,e}$ stands for the radial velocity on an elevation angle level and Δz is the model vertical grid spacing. The function G represents the power gain of the radar beam and is given by

$$G = e^{-z^2/(2\beta^2)}, \qquad (2.9)$$

where z is the distance from the center of the radar beam and β^2 is the beam half-width. The summation is over the model grid points that lie in a radar beam.

In previous versions of VDRAS, radar data were interpolated from the original spherical polar grid to the 3D Cartesian model grid. When comparing the analysis results obtained from the assimilation of the PPI data with the Cartesian data, it was shown that a closer fit to the observations (as defined in each case) was achieved and a smoother analysis produced.

c. Modeling the background error statistics

According to its definition, the background error covariance matrix $\mathbf{B}$ in Eq. (2.6) can be found by taking the expectation value of differences between the true state of the atmosphere and the corresponding background analysis of the field:

$$B_{ij} = \langle (x_i^t - x_i^b)(x_j^t - x_j^b) \rangle. \qquad (2.10)$$

However, it is impossible to define $\mathbf{B}$ directly from its definition unless the true state of the atmosphere is known. Also, it is very difficult to work with a full matrix $\mathbf{B}$ since the matrix is of the order of n^2 where n is the number of 3D grid points in the analysis. For these reasons, simplifications and estimates must be sought to represent the background error statistics. The elements of B can be normalized by the product of standard deviations of the errors at the points i and j to yield the error correlation matrix. In 4DVAR radar data assimilation, the observations are typically sampled at a better resolution than the model resolution and the use of the dynamical model causes the analysis fields to become correlated; hence, the background error covariance plays a less important role than in 3DVAR. Therefore, we have chosen to use a relatively simple correlation model that mainly acts as a filter to smooth out random noise. This correlation model uses a ho-

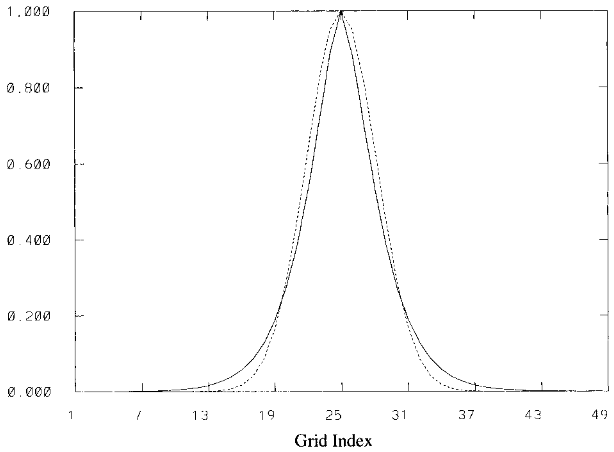

FIG. 1. Distribution of background error correlation after two passes of the filter (solid line) compared with that of a Gaussian function (dashed line).

mogenous horizontal structure function and neglects the vertical correlation. In the following, we first describe how the error correlation is modeled and then how the error variance is specified.

Let $\mathbf{D}$ denote the standard deviation diagonal matrix and $\mathbf{C}$ denote the error correlation matrix. The background error covariance matrix can be written as

$$\mathbf{B} = \mathbf{DCD}. \tag{2.11}$$

Now we employ an exponential function to define the elements of the correlation matrix:

$$\begin{aligned} C_{ij} &= \exp\left(-\frac{|x_i - x_j|}{l_x}\right) \exp\left(-\frac{|y_i - y_j|}{l_y}\right) \\ &= C_{xij}C_{yij}. \end{aligned} \tag{2.12}$$

The matrix $\mathbf{C}$ defined by Eq. (2.12) can be easily inverted because of the separability in x and y. Using the Kronecker product, we have

$$\mathbf{C}^{-1} = \mathbf{C}_x^{-1} \otimes \mathbf{C}_y^{-1}. \tag{2.13}$$

The square roots of $\mathbf{C}_x^{-1}$ or $\mathbf{C}_y^{-1}$ can then be found by a singular vector decomposition (the existence of the square root of the matrix ensures its positive definiteness) and can be truncated to make a banded matrix $\mathbf{F}_x$ or $\mathbf{F}_y$. The background term can now be expressed as

$$J_b = (\mathbf{x}_0 - \mathbf{x}_0^b)^{\mathrm{T}}\mathbf{D}^{-1\mathrm{T}}\mathbf{F}_x^{\mathrm{T}}\mathbf{F}_y^{\mathrm{T}}\mathbf{F}_x\mathbf{F}_y\mathbf{D}^{-1}(\mathbf{x}_0 - \mathbf{x}_0^b). \tag{2.14}$$

The inverted and truncated matrix functions as a recursive filter. If the filter is applied more than once, the resultant error correlation structure (the inversion of $\mathbf{F}_x^{\mathrm{T}}\mathbf{F}_y^{\mathrm{T}}\mathbf{F}_x\mathbf{F}_y$) is pseudo-Gaussian. The error correlation distribution is shown in Fig. 1 for the case of a filter with length scale (l_x, l_y) equal to 2 applied twice in both x and y directions (solid line). Also shown in this plot is the distribution of a Gaussian function centered at $x_0 = 25$ with $2\sigma^2 = 20$ where σ represents the standard deviation.

The main reason for using this error covariance model is its simplicity. However, it should be noted that one needs to be careful when using the method of direct inversion of the structure function. The scaling length has to be substantially smaller than the total number of grid points in the x or y direction. We have found that the scaling length cannot be greater than 4 in order to avoid ill-conditioning of the cost function. Courtier (1997) proposed an incremental 4DVAR algorithm in which the direct inversion of the background error covariance matrix can be avoided by change of control variables. However, the drawback of this algorithm is that the tangent linear model rather than the nonlinear model must be used for the forward integration.

The standard deviation matrix $\mathbf{D}$ is estimated using the radial velocity observations. The radial velocity observations are interpolated to the 3D Cartesian model grid, and then the error variance of the analysis is computed using the observations in the current cycle. This error variance field is used for all the model variables, but a constant scaling factor is applied to the vertical velocity and the potential temperature fields due to the fact that these variables have smaller typical values.

d. Mesoscale analysis

Since radar observations are concentrated within a certain distance of the radar, data voids are often present in the model domain. A background estimate can be used to fill these data voids and to provide a first guess for the minimization procedure. In addition, the background estimate is necessary for specification of the lateral boundary conditions. In our analysis system, the background estimate is provided by combining a velocity azimuthal display (VAD; Lhermitte and Atlas 1961) analysis with a surface mesonet analysis using a least squares fitting technique. The details of the VAD analysis and the mesonet analysis will be given later in this section. This background estimate is used to provide a first guess for the cold start cycle and boundary conditions for the subsequent cycles. The radius of influence in the least squares fitting is set to the distance of one vertical grid point (375 m) on the first level and three grid points on the levels above. We used a smaller length scale in the lowest level in order to maintain the surface wind information as much as possible.

The mesonet analysis is performed using the Barnes interpolation technique (Barnes 1964). Since the Barnes analysis is sensitive to the length of the radius of influence (e.g., Lu and Browning 1998), we have fine-tuned this parameter to make it fit to the data well while giving a smooth analysis. It was found that a value that is 1.5 times of the average spacing (about 16 km) of the observations produced the desired results.

The VAD analysis uses data from the first radar volume in the assimilation window to provide an estimate of the areal-average wind profile, which was first described by Lhermitte and Atlas (1961). They showed

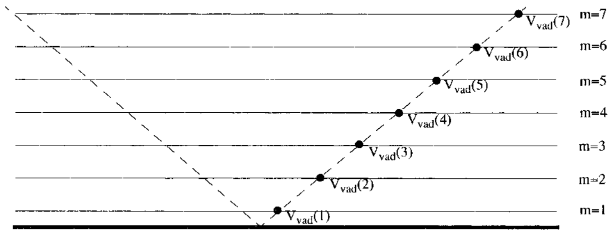

FIG. 2. Sketch of the locations (black dots) where the VAD wind is computed using the PPI VAD method. The solid lines represent the model vertical levels and the dashed line stands for an elevation.

how to determine the mean horizontal wind at any range from the radar as the radar beam sweeps through a full circle. Two schemes of VAD analysis are used in VDRAS. The first scheme is referred to as constant elevation VAD in which the VAD velocity $\mathbf{V}_{\mathrm{VAD}}$ is calculated using data from a constant elevation angle. As illustrated in Fig. 2, data at different ranges from one elevation angle are used to compute the velocity at different heights. The second scheme is referred to as constant range VAD. In this scheme, the PPI 1-km input data are interpolated to the Cartesian grid in the vertical. The VAD velocity at different heights is then calculated at a specified constant range. In section 3, we will compare the performance of these two schemes.

It should be noted that the procedure described above for assimilating mesonet observations is not optimal. A superior technique would be to combine both the radar data and the mesonet observations through the optimization process. Since these two types of observations have significantly different resolutions, a background covariance model that has variable correlation length should be developed. Active research in this area is being conducted (J. Purser 1999, personal communication). We plan to develop a better algorithm for assimilation of mesonet observations in the near future.

e. Lateral boundary conditions

Although it is theoretically possible to retrieve the boundary conditions by including them as control variables, it is practically difficult mainly because of data inadequacy. The boundary conditions of the numerical model are therefore prespecified. The model requires the specification of the horizontal wind at inflow. The outflow boundary conditions are extrapolated using the closest two inner grid points. The lateral boundary conditions of vertical velocity and potential temperature are defined such that their derivatives vanish. In the current version of VDRAS, the inflow boundary conditions are determined by a combination of the along-beam component of the radial velocity observation and the cross-beam component of the background field. On the boundary points where no observations are available, the wind from the mesoscale analysis is used to specify these boundary conditions. We have found that the update of the inflow boundary conditions using the radial velocity observations has a significant impact on the accuracy of the retrieval.

f. Analysis procedure

The 4DVAR analysis is performed using a continuous cycling procedure. The length of the assimilation window in each analysis cycle is 12 min, consisting of three radar volumes in storm mode or two radar volumes in clear air mode. An optimal trajectory is obtained from each cycle using data within the assimilation window. Only the analysis fields at the final time of the assimilation window are written to disk and displayed. These analysis fields are also used as first-guess fields and background in the next analysis cycle. Figure 3 illustrates how the analysis proceeds in time assuming the radar is operating in storm mode. If the analysis system does not find any previous analysis within a specified window (24 min, as in the case of the 4DVAR cycle 1 in Fig. 3), the mesoscale analysis is used as the first guess. In each analysis cycle, an optimal analysis is obtained by minimizing the cost function using a limited-memory quasi-Newton iterative procedure (Liu and Nocedal 1988). In each iteration, the numerical model is integrated forward and the cost function computed. The adjoint model is then integrated backward and the gradient of the cost function is obtained. A practical convergence criterion is to check if $J_m - J_{m-1}$ is smaller

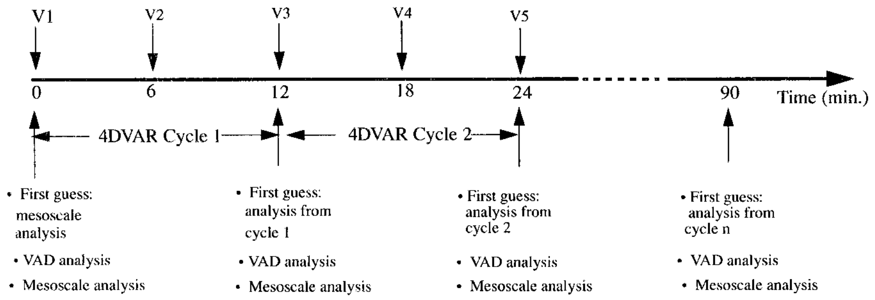

FIG. 3. Illustration of 4DVAR cycles. The radar volumetric input data are shown by the arrows above the time axis. Below the time axis, the first guess and the analyses performed at the beginning of each cycle are described.

than a specified number where *m* represents the iteration number. We have found that as far as real data are concerned, the cost function generally levels out between 30 and 50 iterations. Therefore, in the real-time analysis system, we set the number of iterations to 40.

Radar data are collected through sequential scanning. Although in most traditional radar analysis methods, it is a common practice to assume that the radar volume is a snapshot at a given time, we have shown that the 4DVAR technique is able to assimilate the data at its actual observation time (Sun and Crook 1998; Wu et al. 2000). However, a longer assimilation window is required if the data in each radar volume are assimilated sequentially rather than assuming a single observational time. Let n denote the number of radar volumes to be assimilated in each analysis cycle and Δt the time span of each radar volume, then the assimilation window is $n\Delta t$ for sequential assimilation but $(n - 1)\Delta t$ for single time assimilation. Therefore, in order to save computational time, each radar volume is assimilated by assuming a single observational time.

3. Results

In the 1998 field test, the VDRAS analysis domain covered an area of 150 × 150 km^2 centered at a location southeast of the KLWX radar at Sterling. Since our main focus was to produce boundary layer wind and temperature analyses, a shallow analysis domain with a depth of 2.6 km was used. The second reason for using a shallow domain is computational efficiency. However, when convection is predominant in the analysis domain, the assumption of an impermeable upper boundary is violated. This can lead to spurious results close to the upper boundary if the data covers the entire depth of the domain. If the data cover only the lower portion of the domain, the upper portion of the domain will act as a sponge layer. In both cases, we can still achieve a good fit in the lower levels, which are our main focus in the real-time application. The grid resolution of the analysis domain was 3 km in the horizontal and 375 m in the vertical with a grid mesh of 50 × 50 × 7. Figure 4 shows the analysis domain (thick black square box), the location of the KLWX radar, and the mesonet stations.

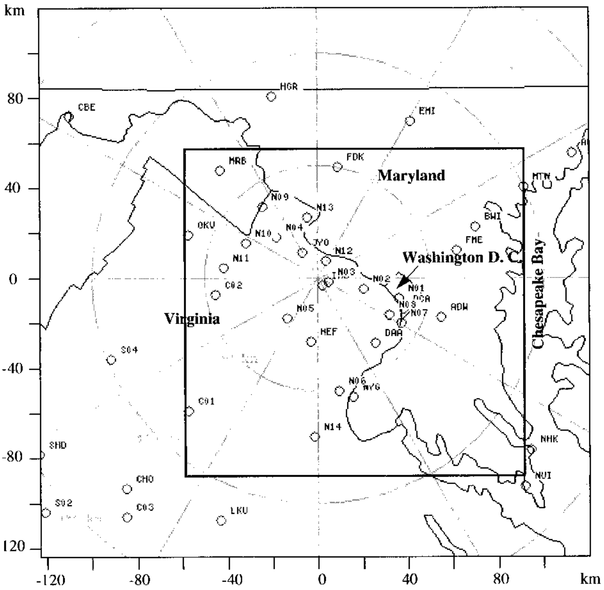

FIG. 4. The VDRAS analysis domain (thick black square) within the nowcasting domain. The position of the KLWX radar, the state borders, and the mesonet stations are also shown.

During the summer of 1998, the WSR-88D radar at Sterling observed several severe storm events. Most of these were associated with strong boundary layer convergence zones that VDRAS successfully retrieved. After the field test, a number of new developments (described in section 2) were incorporated into the analysis system. The archived Sterling 1998 data were reexamined and several periods in which severe weather occurred were rerun. The results from these cases were verified using ACARS data from flights taking off and landing at Dulles International Airport. Verification results will be presented in the next section. In this section, we present results from one case that occurred in the afternoon of 15 June 1998.

On the afternoon of 15 June 1998, a line of storms moved into the analysis domain around 1900 UTC. As the storm system propagated toward the southeast, a new initiation of storms took place along the thunderstorm outflow and strong northwesterly winds developed. There were a number of reports of wind damage in Charles County, about 30 km south of Washington D.C. In Fig. 5, the observed reflectivity field at an interval of around 30 min is presented. It is evident that the storm went through a rapid development from 2026 (Fig. 5a) to 2057 UTC (Fig. 5b) and then propagated southeastward at a speed of around 13 m s^{-1}.

We ran VDRAS starting from 1934 UTC, which is shortly after the storm system moved into the analysis domain. An analysis was produced approximately every 11 min (the time between radar volume scans was about 5.5 min during this period) for a period of about 3 h consisting of 16 4DVAR analysis cycles. In each analysis cycle, the minimization was halted at 50 iterations. In the rest of this section, we will first show results from a control experiment and then present a number of experiments that were conducted to examine the sensitivity of the analysis system to the background term, the exclusion of mesonet and reflectivity data, VAD analysis schemes, and the penalty term. Table 1 lists all the experiments presented in this paper. To compare the quality of these retrieval experiments, a 90-min forecast was performed starting with the analysis at 2108 UTC. Forecast velocity fields were then verified against the observed radial velocity.

Both radial velocity and reflectivity data are used in

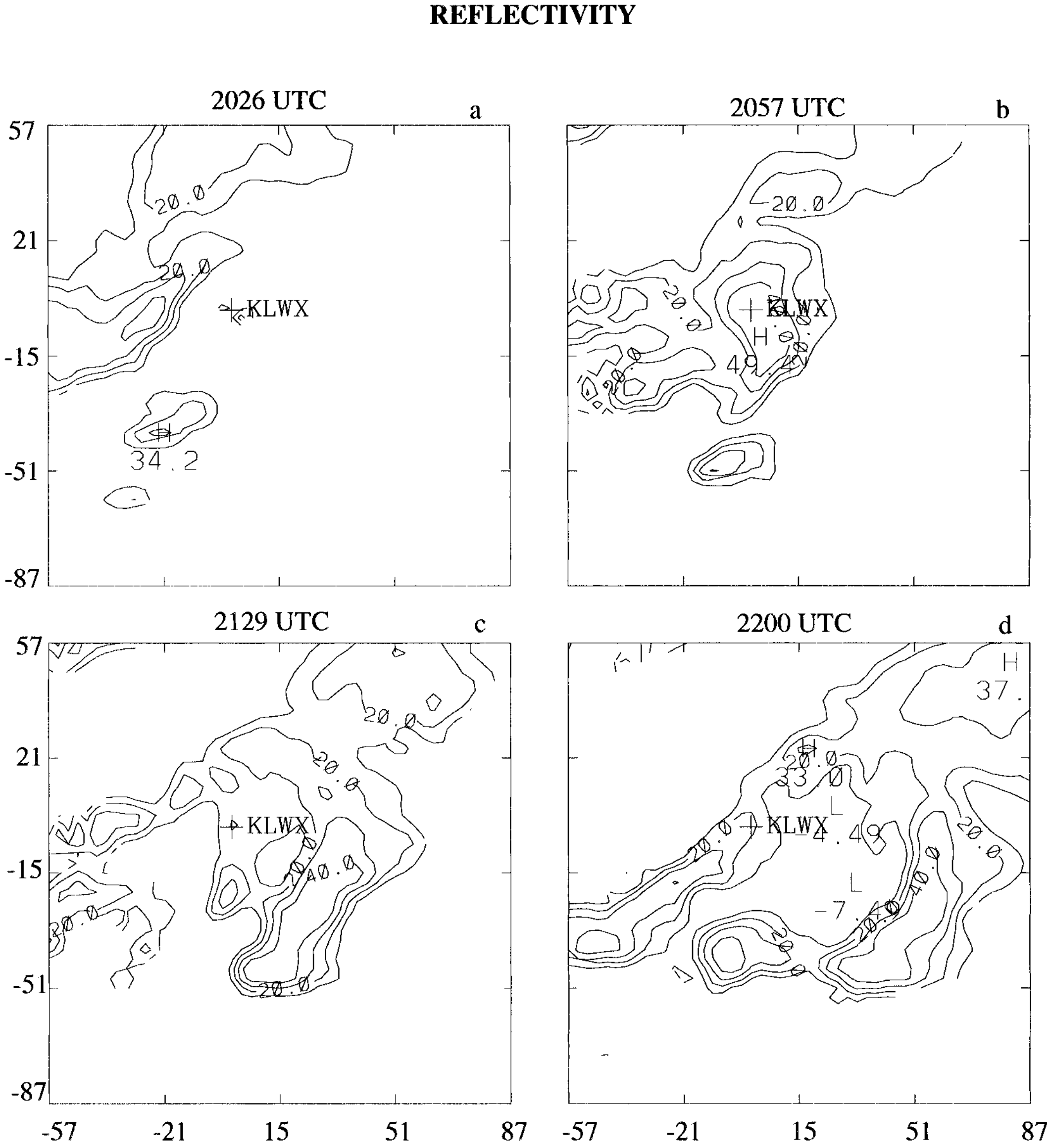

FIG. 5. Reflectivity at the 0.5° elevation angle. The contour interval is 10 dBZ. The location of the KLWX radar is also shown.

the control experiment. Continuous assimilation cycles are performed in which the analysis from the previous cycle is used as the background. The inflow boundary conditions are given by a combination of the background wind and the radial velocity observations as described in section 2e. The coefficients α_3 and α_4 are set to 0.005 for the horizontal velocity components and 0.01 for the vertical velocity and temperature. The coefficients α_1 and α_2 are set to the same value on the boundaries and zero otherwise. The choice of these penalty coefficients was determined empirically. Fortunately, the retrieval is not especially sensitive to these values as long as they are within certain ranges because the penalty term plays a secondary role compared to the observation term (Sun 1992). As a principle, the penalty

TABLE 1. Experiment summary.

Expt no.	Description
1	Control experiment
2	A forecast cycle follows each analysis cycle
3	PPI VAD analysis is used for mesoscale background
4	No mesonet data
5	No reflectivity data
6	Observation term only
7	No penalty term
8	No background term

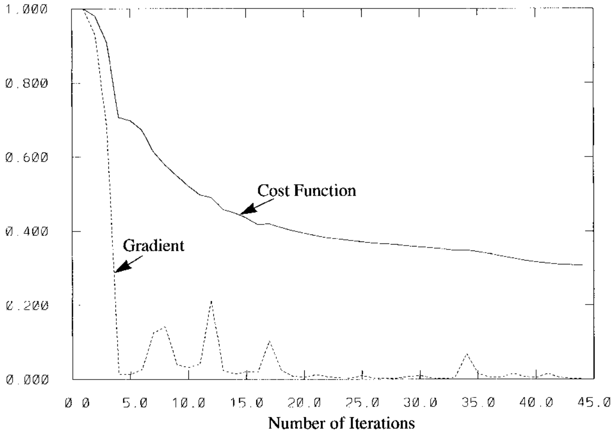

FIG. 6. Reduction of the cost function (solid line) and the gradient (dashed line) with respect to the number of iterations.

coefficients should be as large as possible to suppress random noise but not so large that it dominates the cost function. The values of the penalty coefficients were used for all of the experiments presented here and in the real-time operation during the summer of 1998. Figure 6 shows the reduction of the cost function (solid curve) and the gradient (dashed curve) with respect to the number of iterations in the control experiment. The plotted data are from one of the 16 analysis cycles, but they are representative of the behavior of the minimization process in all of the cycles. The cost function is reduced by more than 70% of its first-guess value and the gradient is reduced by two orders of magnitude of its first-guess value. Although the reduction of the cost function and the gradient varies in different experiments, we have found that the convergence behavior is rather similar and no problems in convergence were experienced in any of the experiments conducted.

The evolution of the low-level horizontal divergence field calculated from the retrieved wind is shown in Fig. 7 and the retrieved temperature perturbation (from the horizontal mean) field plotted in Fig. 8. The retrieved horizontal wind vector field is overlaid on these plots. As can be seen from Fig. 8, a cold pool with a maximum cooling of 1.8°C is retrieved at 2057 UTC. The cold pool produced northwesterly winds and strong convergence along the leading edge of the gust front. It is seen that the temperature perturbation field is highly correlated with the horizontal divergence field. This is typical for nonhydrostatic flows as implied by the equations of motion. One of the distinct features of VDRAS is the temporal continuity of the retrieved fields as exhibited in Fig. 7, which is primarily due to the use of the dynamical model. This temporal continuity is important for forecasting of the low-level flow.

While the VDRAS analysis shows strong convergence along the leading edge of the gust front, the mesoscale analysis at 2129 UTC (Fig. 9a) does not show any of the gust front features (although the wind vector in the northern half of the analysis domain does turn from southwesterly to westerly). A slightly more detailed mesoscale analysis field can be obtained by reducing the radius of influence, but noise tends to appear in the regions where the mesonet stations are sparse. Although a more advanced technique such as the three-dimensional variational analysis might be able to generate a better mesoscale analysis than that shown in Fig. 9a, the degree of detail in the analysis is limited by the resolution of the mesonet observations. The high resolution of the radar observations combined with the four-dimensional variational analysis technique enables us to capture more detail in the gust front structure. The difference vector between the retrieved wind and the mesoscale analysis wind (Fig. 9a) is presented in Fig. 9b. It shows that the modification of the wind occurs largely in the region behind the leading edge of the gust front.

The difference vector as shown by Fig. 9b can be decomposed into radial and tangential components relative to the radar. Although the radial component is a close fit to the radial velocity observation, any tangential component must be derived through the retrieval process. To examine the contribution of the retrieved tangential component to the difference vector, the root-mean square (rms) of the radial and tangential winds at each vertical level at 2129 UTC is plotted in Fig. 10a. This shows that the correction resulting from the tangential component is substantial. To further examine the tangential wind contribution in the storm outflow region (defined as the region where the perturbation temperature is less than 0°C), in Fig. 9c, the difference vectors in this subarea are plotted with the observed radial velocity subtracted. The rms of the radial and tangential winds in the storm outflow subarea are plotted in Fig. 10b and the rms of the radial and tangential components of the 2D polar divergence are plotted in Fig. 10c. The greater difference between the radial and tangential winds in this subarea is most likely the result of the particular flow pattern associated with the curved leading edge of the cold air that developed right at the radar (Fig. 8b).

A forecast starting from the retrieved fields at 2108 UTC was conducted. The radial velocity from the forecast is then interpolated to the grid of the radial velocity observations and the rms error calculated. The boundary conditions at the initial time were applied throughout the entire forecast period. The radial velocity rms error from the forecast is shown by the solid curve in Fig. 11. The long dashed curve labeled persistence in this figure displays the rms error between the observed radial velocity and the radial velocity at the initial time (2108 UTC). The short dashed curve labeled mesoscale initialization shows the rms error of the forecast starting from the mesoscale analysis. As can be seen the forecast from the radar data initialization outperforms the forecast from the mesoscale initialization and persistence (except for the first ~10 min).

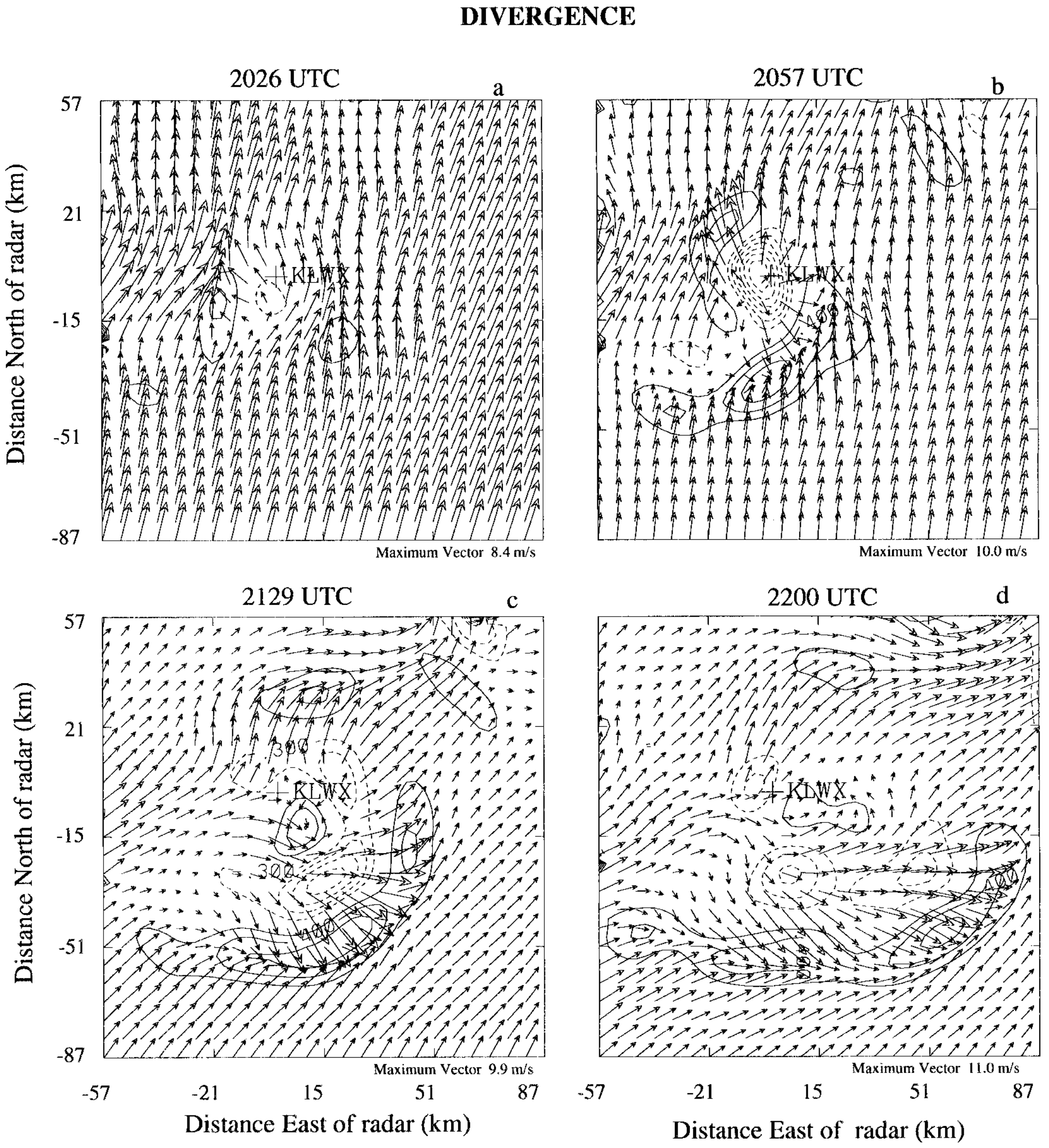

FIG. 7. Horizontal divergence calculated from the retrieved wind overlaid by the retrieved velocity vectors at $z = 0.187$ km. Solid line indicates convergence and dashed line divergence. A scaling of 10^5 s^{-1} is applied to the contour values.

The use of the analysis background produces a correlation between the background term and the observation term and this correlation is neglected in the 4DVAR computation. To circumvent this problem, each analysis cycle can be followed by a short forecast that can be used as the background in the next analysis cycle, as in experiment 2. Compared with the control experiment, the analysis rms error in radial velocity in experiment 2 is greater (2.40 vs 2.10 m s^{-1}). In Fig. 12, the forecast rms error from this experiment is shown and compared with that from the control experiment.

In section 2, we discussed the two VAD analysis schemes, constant range VAD (used in the control experiment) and constant elevation VAD. In experiment 3, we use the constant elevation VAD profile to test the sensitivity of the analysis to the VAD calculation. Figure 13 shows the velocity profiles obtained from the two VAD techniques. The profile calculated using the constant range VAD is smoother than that using the constant elevation VAD. The forecast using the initial fields obtained from experiment 3 is shown in Fig. 14 (long and short dashed line) and compared with that from the control experiment. The forecast shows a significant degradation when the constant elevation VAD is used in spite of the fact that the analysis at the initial time of the forecast period has slightly smaller error than that in the control experiment.

High-resolution mesonet observations are not avail-

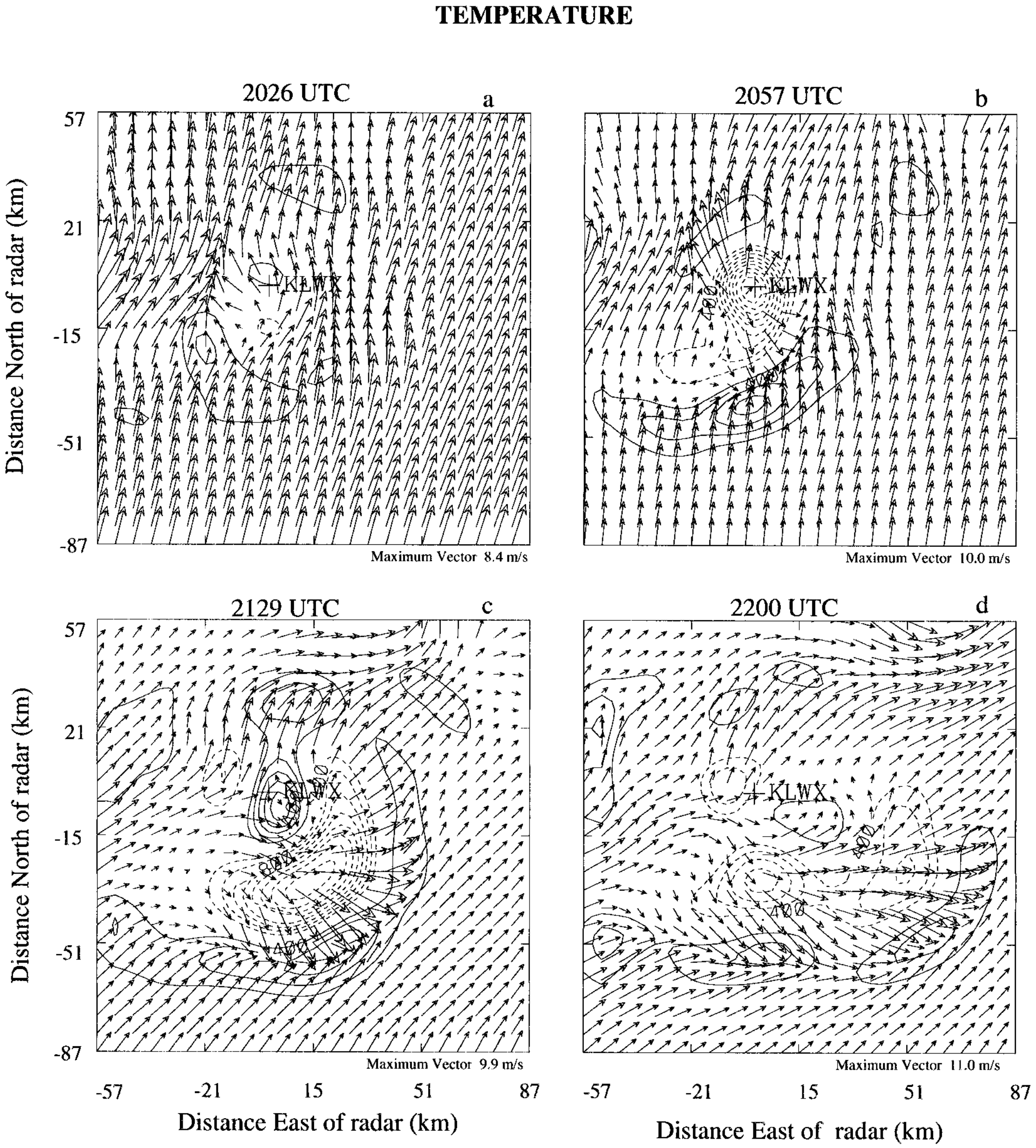

FIG. 8. Retrieved temperature field overlaid with the retrieved velocity vectors at z = 0.187 km. The contour interval is 0.2°C. Negative values are dashed lines and positive values are solid lines.

able everywhere throughout the United States. When there are no mesonet observations, the mesoscale analysis depends solely on the VAD analysis. To examine how sensitive VDRAS is to the mesonet data, we excluded the mesonet data in experiment 4. The forecast starting from this analysis shows a degradation throughout the entire forecast period although the degradation is not very significant (see the short dashed line in Fig. 14).

A similar experiment, experiment 5, was performed to test the sensitivity of the analysis with respect to the exclusion of the reflectivity observations. As shown by the long dashed curve in Fig. 14, the retrieval is not very sensitive to the exclusion of reflectivity data. To further determine the effect of the reflectivity data, an experiment that uses only reflectivity and no radial velocity data was conducted. It was found that the retrieved velocity amplitude was much smaller and the gust front structure was not well captured in this experiment.

One of the major challenges in radar data analysis is to produce an analysis with a smooth transition between regions with and without radar data. Although some other types of observations may be available in the radar data-void region, these data usually have much poorer resolution than the model resolution. A good analysis should be able to fit to the observations while maintaining a smooth field especially in the area where ob-

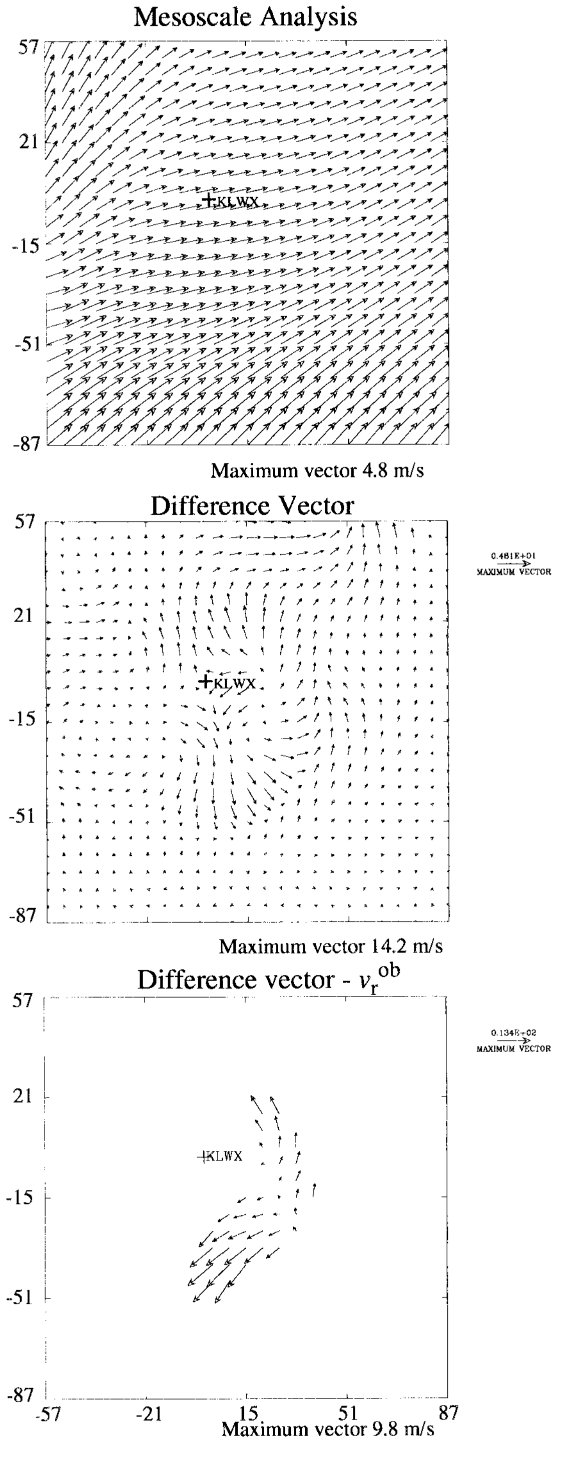

FIG. 9. Horizontal wind vector at $z = 0.187$ km at 2129 UTC. (a) Mesoscale analysis, (b) difference vector between VDRAS analysis and mesoscale analysis, and (c) similar to (b) but the observed radial velocity is subtracted and only the storm outflow region is plotted.

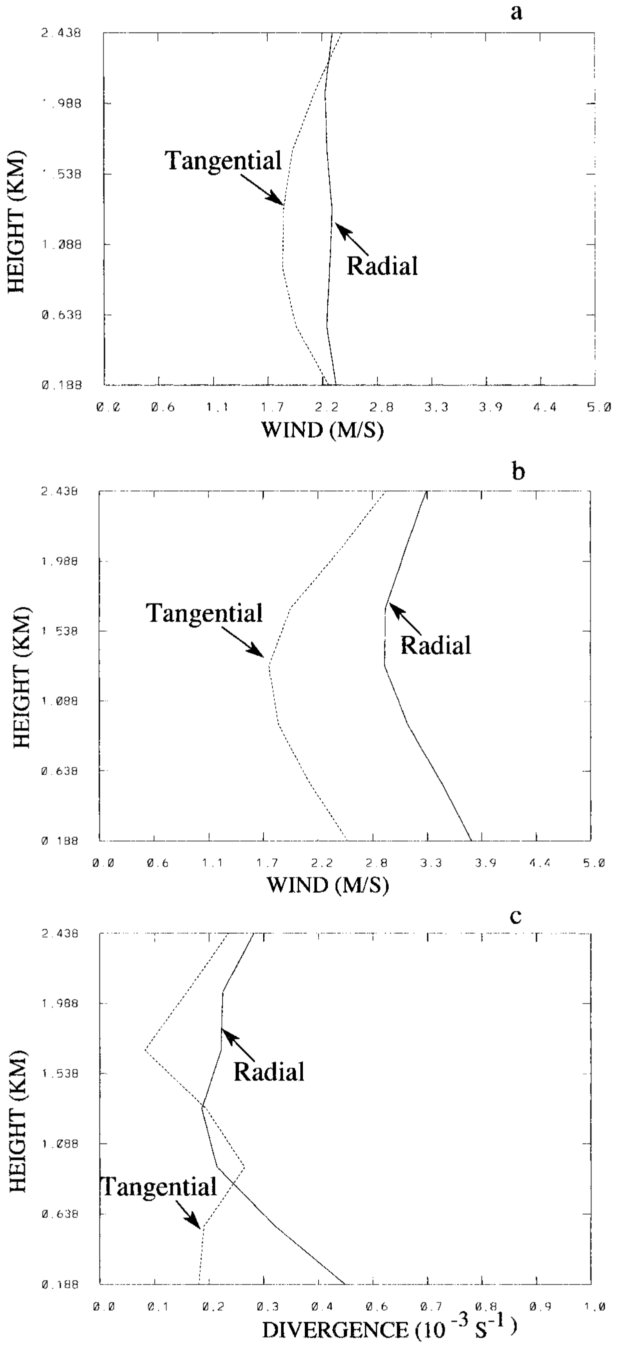

FIG. 10. (a) Rms of radial velocity and tangential velocity of the difference vector as shown in Fig. 9b, (b) same as (a) but only for the storm outflow region, and (c) rms of radial and tangential divergence in the storm outflow region.

servations are sparse. Both the background term and the penalty term in the cost function can help to smooth the analysis. In the next experiments, we test the impact of these terms on the analysis and forecast. In experiment 6, both these terms are excluded. This experiment has the smallest analysis error (1.38 m s^{-1}) among all of the experiments presented here. However, the subse-

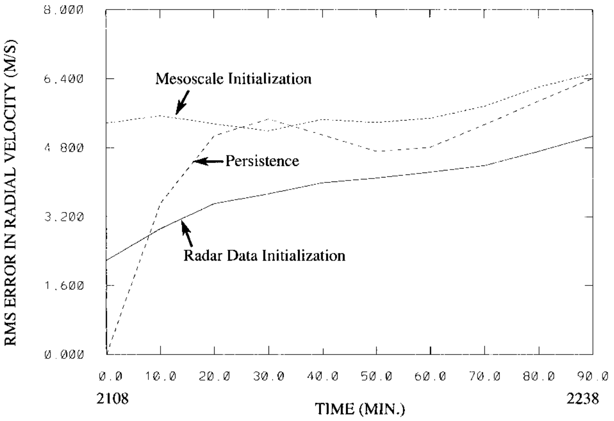

FIG. 11. Forecast rms error for the control experiment.

quent forecast shows much larger errors (short dashed curve in Fig. 15) than the control experiment. An examination of the analysis fields from this experiment (not shown) indicated the development of noise in the region without radar data.

To compare the effect of the background term with the penalty term, experiments 7 and 8 were conducted. In experiment 7, only the background term is used while experiment 8 uses only the penalty term. The forecast errors from these two experiments are shown by the long-and-short-dashed curve (experiment 7) and long dashed curve (experiment 8) in Fig. 15. Although the two terms perform quite well separately, the best forecast is obtained when both terms are included in the control experiment.

The penalty term works quite effectively to suppress random noise in the optimization process. Its advantage compared to the background term is that it does not depend on the quality of the background field. However, its disadvantage is that the weighting coefficients have to be determined from experience. Nevertheless, we have found that the analysis and the subsequent forecast are not very sensitive to the magnitude of the weighting coefficients within a range of a few orders of magnitude.

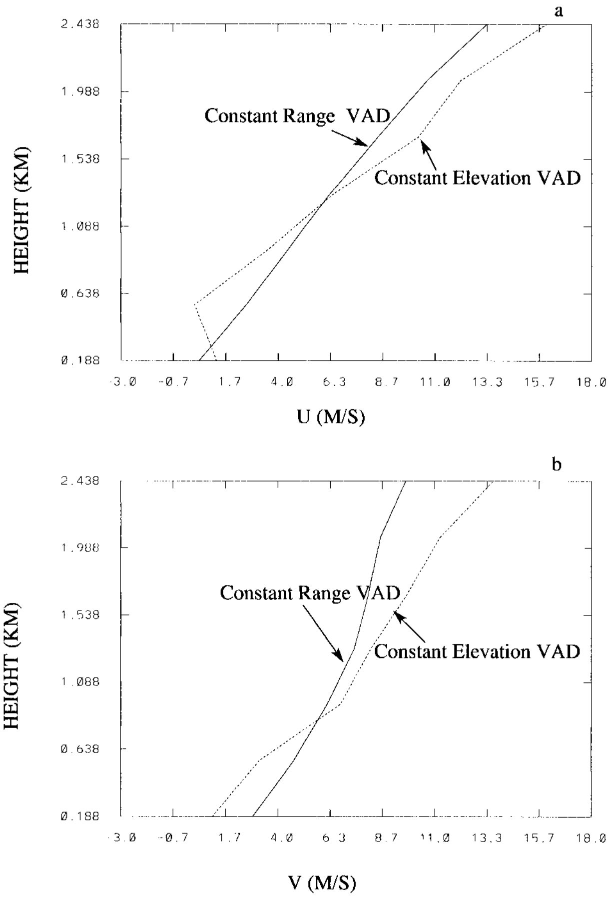

FIG. 13. Velocity profiles obtained from the two VAD analysis methods: (a) *U* and (b) *V*.

Another disadvantage of the penalty term is that it only smooths the analysis within a distance of a few grid points because it uses second-order derivatives. In comparison with the penalty term, a background term with a good model of error statistics holds more promise since the filtering performed through the use of an ap-

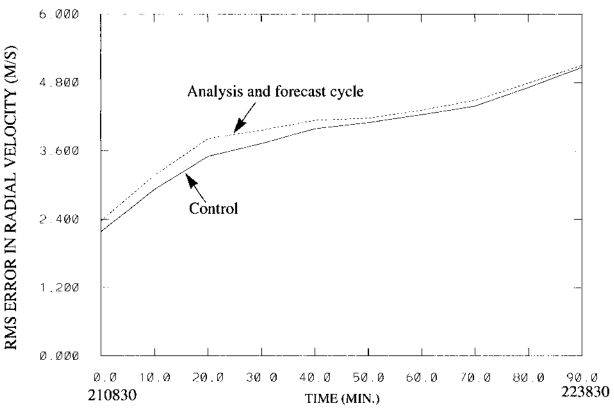

FIG. 12. Forecast rms error for experiments 1 and 2.

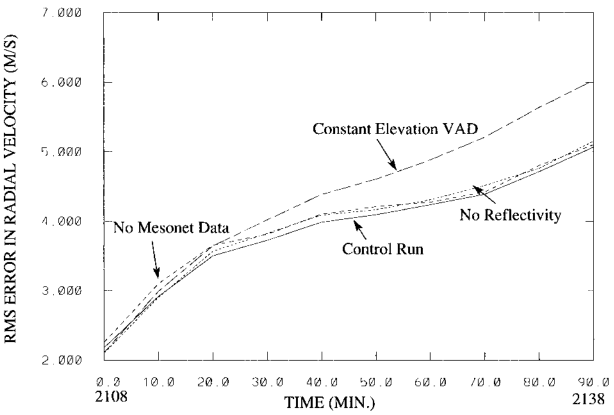

FIG. 14. Forecast rms error for experiments 1, 3, 4, and 5.

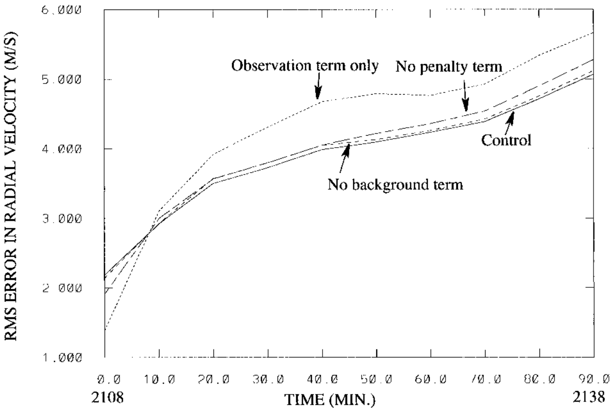

FIG. 15. Forecast rms error for experiments 1, 6, 7, and 8.

propriate error correlation, for example with a variable length scale, can provide more flexibility.

4. Verification using ACARS data

ACARS data from flights taking off and landing at Dulles International Airport (~5 km southeast of KLWX) are used to verify the wind analyses. The temperature is not used for verification because VDRAS produces temperature perturbation rather than the absolute temperature as in the ACARS observation. The mean temperature used in VDRAS is from the radiosonde observations at a nearby station that are available every 12 h. If this mean temperature is used to compute the absolute temperature, the error can be easily 1°C, which is the magnitude of the perturbation temperature in the boundary layer. The ACARS observations are located at heights of approximately 600, 1200, and 1800 m. To compare an analysis with an ACARS observation, the gridded wind from the analysis is interpolated to the ACARS observation location and then the mean vector difference (MVD) is calculated:

$$\mathrm{MVD} = \frac{1}{N}\sum \sqrt{(u - u_{\mathrm{ac}})^2 + (v - v_{\mathrm{ac}})^2}, \qquad (4.1)$$

where u_{ac} and v_{ac} represent ACARS velocities and N is the total number of ACARS observations. Table 2 lists the verification results for six days when severe weather occurred within the analysis domain. For most of the cases, we ran the analysis system for 3 h. In Table 2, the MVD of the VDRAS analysis is listed in the third column. To show the improvement of the VDRAS analysis over the mesoscale analysis, the MVD of the mesoscale analysis is listed in the second column. Also shown in Table 2 is the rms radial velocity difference between the ACARS observation and the radar observation, which gives a measure of both instrumentation error and error of representativeness. This difference is calculated by comparing the ACARS radial velocity computed from the observed horizontal velocity components u_{ac} and v_{ac} and the radial velocity interpolated to the ACARS measurement point. The last column displays the value of the average wind from the ACARS measurement in order to provide a relative estimate of the analyses.

The parameter settings of the six cases follow that in the control simulation described in the last section. It should be noted that the smallest MVD of the VDRAS analysis can be found from experiment 6 in which both the penalty and background terms are turned off. However, as discussed in the last section, this experiment gives a worse forecast. Therefore, caution must be exercised in verifying the analysis using limited observations. Since our ultimate goal is to produce an analysis that gives the best forecast, we used the control simulation for the verification. From the statistics shown in Table 2, we can see that the averaged MVD in the VDRAS analysis is 3.3 m s^{-1}, while the MVD of the mesoscale analysis is 4.8 m s^{-1} and the rms radial velocity difference is 2.3 m s^{-1}. The VDRAS outperforms the mesoscale analysis for all of the six cases. It is interesting to note that the two cases that have the largest relative difference in the VDRAS analysis (comparing column 3 with column 5) also reveal the largest relative difference in the observed radial velocity (comparing column 4 with column 5). We have also found that a large portion of the VDRAS analysis error is in the tangential component, which is not surprising because the radial component is observed and a best fit to these observations is achieved in the analysis.

The difference between the ACARS wind and the VDRAS wind can be attributed to a number of reasons such as the inaccurate boundary conditions, error in both observations, representativeness of the VDRAS analysis

TABLE 2. Verification using ACARS data.

Date	MVD (mesoscale analysis, in m s^{-1})	MVD (VDRAS analysis, in m s^{-1})	RMS radial velocity difference (m s^{-1})	Average ACARS wind (m s^{-1})
15 Jun 1998	8.8	4.9	1.6	10.4
16 Jun 1998	5.2	3.8	2.3	6.4
24 Jun 1998	4.1	3.3	2.7	4.6
30 Jun 1998	3.8	2.6	3.4	16.2
21 Jul 1998	3.7	3.0	2.2	8.6
31 Jul 1998	3.7	2.4	1.3	8.4
All days	4.8	3.3	2.3	9.1

versus the ACARS observation, and model error. A major source of the model error is the neglect of the microphysical processes. At low levels, the process that has the most impact is the evaporation of rain. As an interim step before computational resources allow us to run a complete cloud model, we plan to add an evaporation scheme to the model in the near future.

5. Summary and conclusions

A 4DVAR radar data analysis system for low-level wind and temperature retrieval was implemented at a weather forecast office to produce real-time low-level wind and temperature analyses using WSR-88D radar observations. The system ran continuously through the summers of 1998 and 1999 with little human intervention. A 4DVAR cycling analysis procedure was implemented in which the analysis from the previous cycle was used as a background and first guess for the subsequent cycle. Several other new features were added to the system before, during, and after these field tests to make the system work robustly with real data. Among these new features are the direct assimilation of PPI data, the mesoscale analysis, and continuous updating of the lateral boundary conditions.

A case of a line of storms was used to demonstrate the performance of the analysis system. The analysis shows a low-level gust front characterized by strong wind, convergence, and a cold pool. A 90-min forecast initialized by the VDRAS analysis outperforms persistence and a forecast initialized by the mesoscale analysis. Several sensitivity experiments are conducted and the performance compared using the subsequent forecast. The main conclusions from the sensitivity study are summarized in the following:

1) Using the analysis from the previous cycle for a background field yields better results than using a short forecast. The neglect of the correlation between the previous analysis and the observations does not appear to significantly impact the current analysis.
2) The VAD computed at constant range yields a smoother velocity profile than the VAD computed at a constant elevation angle. As a result, a better forecast is obtained using the constant range VAD.
3) Exclusion of mesonet data or reflectivity data degrades the analysis and the forecast only slightly. This suggests that the radial velocity data plays the major role in the retrieval.
4) Both the background term and the penalty term serve to produce an analysis that has a smooth transition between the data-dense and data-sparse regions. We have found that the best result is obtained by using both terms.

ACARS data from flights taking off and landing at Dulles International Airport are used to verify the six cases with severe weather. Verification shows that VDRAS outperforms the mesoscale analysis for all six cases. The average MVD in the VDRAS analysis is 3.3 m s^{-1} compared to 4.8 m s^{-1} for the mesoscale analysis.

VDRAS has been implemented in the weather forecast office in Sydney, Australia, along with the Auto-Nowcaster for field testing aimed at providing real-time nowcasting for the summer Olympics in September 2000. Along with the field testing, we have commenced a number of projects aimed at improving the analysis system. A collaborative study to develop a set of observation error statistics is being conducted. The error statistics will be generated based on signal-to-noise ratio and spectrum width. A more sophisticated background error covariance model that combines several Gaussian distribution functions (J. Purser 1999, personal communication) will also be implemented and tested in the near future.

Acknowledgments. The authors would like to thank Jay Miller and Rita Roberts for their review of the manuscript. We are very grateful to Doug Nychka for his help in developing the background error statistics model. Thanks are due to Jim Wilson and Rita Roberts for their support in the real-time testing of the system. We are also very grateful to Terri Betancourt and Jaimi Yee for their engineering support. This work is funded by the FAA and the National Science Foundation.

REFERENCES

Barnes, S., 1964: A technique for maximizing details in numerical map analysis. *J. Appl. Meteor.*, **3,** 395–409.

Courtier, P., 1997: Dual formulation of four dimensional variational assimilation. *Quart. J. Roy. Meteor. Soc.,* **123,** 2449–2461.

——, and O. Talagrand, 1987: Variational assimilation of meteorological observations with the adjoint vorticity equation. Part II: Numerical results. *Quart. J. Roy. Meteor. Soc.,* **113,** 1329–1347.

Gal-Chen, T., 1978: A method for the initialization of the anelastic equations: Implications for matching models with observations. *Mon. Wea. Rev.,* **106,** 587–606.

Gao, J., M. Xue, Z. Wang, and K. K. Droegemeier, 1998: The initial condition and explicit prediction of convection using ARPS adjoint and other retrieval methods with WSR-88D data. Preprints, *12th Conf. on Numerical Weather Prediction,* Phoenix, AZ, Amer. Meteor. Soc., 176–178.

Hane, C. E., and B. C. Scott, 1978: Temperature and pressure perturbations within convective clouds derived from detailed air motion information: Preliminary testing. *Mon. Wea. Rev.,* **106,** 654–661.

Jing, Z., and G. Wiener, 1993: Two-dimensional dealiasing of Doppler velocities. *J. Atmos. Oceanic Technol.,* **10,** 798–808.

Laroche, S., and I. Zawadsky, 1994: A variational analysis method for the retrieval of three-dimentional wind field from single-Doppler data. *J. Atmos. Sci.,* **51,** 2664–2682.

Le Dimet, F. X., and O. Talagrand, 1986: Variational algorithms for analysis and assimilation of meteorological observations: Theoretical aspects. *Tellus,* **38A,** 97–110.

Lewis, J. M., and J. C. Derber, 1985: The use of adjoint equation to solve a variational adjustment problem with advective constraints. *Tellus,* **37A,** 309–322.

Lhermitte, R. M., and D. Atlas, 1961: Precipitation motion by pulse Doppler radar. *Proc. Ninth Weather Radar Conf.,* Kansas City, MO, Amer. Meteor. Soc., 218–223.

Liou, Y.-C., 1990: Retrieval of three-dimensional wind and temperature fields from one component wind data by using the four-dimensional data assimilation technique. M. S. thesis, Department of Meteorology, University of Oklahoma, 112 pp. [Available from Department of Meteorology, University of Oklahoma, 100 E. Boyd, Rm 1310, Norman, OK 73019.]

Liu, D. C., and J. Nocedal, 1988: On the limited memory BFGS method for large scale optimization. Tech. Rep. NAM 03, Department of Electrical Engineering and Computer Science, Northwestern University, Evanston, IL, 26 pp. [Available from Department of Electrical and Computer Engineering, Northwestern University, 2145 Sheridan Road, Evanston, IL 60208.]

Long, R. B., and W. C. Thacker, 1989: Data assimilation into a numerical equatorial ocean model: Part 2: Assimilation experiments. *Dyn. Atmos. Oceans,* **13,** 413–439.

Lu, C., and G. L. Browning, 1998: The impact of observational errors on objective analyses. *J. Atmos. Sci.,* **55,** 1791–1807.

Rinehart, R. E., 1979: Internal storm motions from a single non-Doppler weather radar. NCAR TN-146 + STR, NCAR, Boulder, CO, 262 pp.

Roberts, R., T. Saxon, C. Mueller, J. Wilson, A. Crook, J. Sun, and S. Henry, 1999: Operational application and use of NCAR's thunderstorm nowcasting system. Preprints, *15th Int. Conf. on Interactive Information and Processing Systems for Meteorology, Oceanography, and Hydrology,* Dallas, TX, Amer. Meteor. Soc., 158–161.

Shapiro, S., S. Ellis, and J. Shaw, 1995: Single-Doppler velocity retrievals with Phoenix II data: Clear air and microburst wind retrievals in the planetary boundary layer. *J. Atmos. Sci.,* **52,** 1265–1287.

Sun, J., 1992: Convective scale 4-D data assimilation using simulated single-doppler radar observations. Ph.D. dissertation, University of Oklahoma, 174 pp. [Available from Department of Meteorology, University of Oklahoma, 100 E. Boyd, Rm 1310, Norman, OK 73019.]

——, and N. A. Crook, 1994: Wind and thermodynamic retrieval from single-Doppler measurements of a gust front observed during Phoenix II. *Mon. Wea. Rev.,* **122,** 1075–1091.

——, and ——, 1997: Dynamical and microphysical retrieval from Doppler radar observations using a cloud model and its adjoint. Part I: Model development and simulated data experiments. *J. Atmos. Sci.,* **54,** 1642–1661.

——, and ——, 1998: Dynamical and microphysical retrieval from Doppler radar observations using a cloud model and its adjoint. Part II: Retrieval experiments of an observed Florida convective storm. *J. Atmos. Sci.,* **55,** 835–852.

——, D. W. Flicker, and D. K. Lilly, 1991: Recovery of three-dimensional wind and temperature fields from single-Doppler radar data. *J. Atmos. Sci.,* **48,** 876–890.

Talagrand, O., and P. Courtier, 1987: Variational assimilation of meteorological observations with the adjoint vorticity equation—Part I. Theory. *Quart. J. Roy. Meteor. Soc.,* **113,** 1311–1328.

Telesetsky, W., 1995: Current status and issues of the Weather Surveillance Radar-1988 Doppler program. Preprints, *26th Int. Conf. on Radar Meteorology,* Vail, CO, Amer. Meteor. Soc., XXXVIII.

Tuttle, J. D., and G. B. Foote, 1990: Determination of the boundary-layer airflow from a single Doppler radar. *J. Atmos. Oceanic Technol.,* **7,** 218–232.

Wahba, G., and J. Wendelberger, 1980: Some new mathematical methods for variational objective analysis using spline and cross-validation. *Mon. Wea. Rev.,* **108,** 1122–1143.

Warner, T. T., E. E. Brandes, C. K. Mueller, J. Sun, and D. N. Yates, 2000: Prediction of a flash flood in complex terrain. Part I: A comparison of rainfall estimates from radar, and very short range rainfall simulations from a dynamic model and an automated algorithmic system. *J. Appl. Meteor.,* **39,** 797–814.

Weygandt, S., 1998: The retrieval of initial forecast fields from single-Doppler observations of a supercell thunderstorm. Ph.D. dissertation, University of Oklahoma, 257 pp. [Available from Department of Meteorology, University of Oklahoma, 100 E. Boyd, Rm 1310, Norman, OK 73019.]

Wolfsberg, D., 1987: Retrieval of three-dimensional wind and temperature fields from single-Doppler radar data. CIMMS Rep. 84, 91 pp. [Available from Cooperative Institute for Mesoscale Meteorological Studies, 401 East Boyd, 100 East Boyd St., Norman, OK 73019.]

Wu, B., J. Verlinde, and J. Sun, 2000: Dynamical and microphysical retrieval from Doppler radar observations of a deep convective cloud. *J. Atmos. Sci.,* **57,** 262–283.

Xu, Q., C.-J. Qiu, J.-X. Yu, H.-D. Gu, and M. Wolfson, 1993: Adjoint method retrievals of microburst winds from TDWR data. Preprints, *26th Int. Conf. on Radar Meteorology,* Norman, OK, Amer. Meteor. Soc., 433–434.

Zhang, J., and T. Gal-Chen, 1996: Single-Doppler wind retrieval in the moving frame of reference. *J. Atmos. Sci.,* **53,** 2609–2623.